BBA - Bioenergetics 1860 (2019) 89–101

Contents lists available at ScienceDirect

BBA - Bioenergetics

journal homepage: www.elsevier.com/locate/bbabio

Measuring the functionality of the mitochondrial pumping complexes with multi-wavelength spectroscopy

Mariana Rocha, Roger Springett*

Cardiovascular Division, King's College London, British Heart Foundation Centre of Excellence, 125 Coldharbour Lane, London SE5 9NU, United Kingdom

ARTICLE INFO

Keywords:
Electron transport chain
Proton pumping
ATP
Equilibrium
Free energy
Turnover

ABSTRACT

The proton pumps of the mitochondrial electron transport chain (ETC) convert redox energy into the proton motive force (Δ*P*), which is subsequently used by the ATP synthase to regenerate ATP. The limited available redox free energy requires the proton pumps to operate close to equilibrium in order to maintain a high Δ*P*, which in turn is needed to maintain a high phosphorylation potential. Current biochemical assays measure complex activities far from equilibrium and so shed little light on their function under physiological conditions. Here we combine absorption spectroscopy of the ETC hemes, NADH fluorescence spectroscopy and oxygen consumption to simultaneously measure the redox potential of the intermediate redox pools, the components of Δ*P* and the electron flux in RAW 264.7 mouse macrophages. We confirm that complex I and III operate near equilibrium and quantify the linear relationship between flux and disequilibrium as a metric of their function under physiological conditions. In addition, we quantify the dependence of complex IV turnover on Δ*P* and the redox potential of cytochrome *c* to determine the complex IV driving force and find that the turnover is proportional to this driving force. This form of quantification is a more relevant metric of ETC function than standard biochemical assays and can be used to study the effect of mutations in either mitochondrial or nuclear genome affecting mitochondrial function, post-translation changes, different subunit isoforms, as well as the effect of pharmaceuticals on ETC function.

1. Introduction

In Mitchell's hypothesis of oxidative phosphorylation, protons pumped across the inner mitochondrial membrane by the electron transport chain (ETC) generate a proton motive force (ΔP) which drives the regeneration of ATP by the F1Fo ATPase synthase [1]. The proton/electron stoichiometry of the pumps and the ATP/H^+ stoichiometry of both the ATP synthase [2] and ATP transport circuit [3] are fixed with little slip or leak [4] and therefore the rate of ATP production is tightly coupled to the rate of oxygen consumption. ATP must be produced not only at the rate needed by cytosolic ATP consuming processes but also, importantly, at a high phosphorylation potential (ΔG_{ATP}) so that these consuming processes are driven in the forward direction; the importance of maintaining ΔG_{ATP} high is demonstrated in the mammalian heart which can alter its oxygen consumption and ATP production by several fold while maintaining ΔG_{ATP} essentially constant [5]. From a thermodynamic perspective, oxidative phosphorylation can be viewed as an energy transduction process in which redox free energy is first converted into a proton motive force by the electron transport chain and then into the cytosolic phosphorylation potential by the ATP synthase and transport proteins. The free energy change (Δ*G*) of a proton pump, expressed in Joules per mole of electrons transferred, is given by:

$$\Delta G = -F\Delta E_S + F\Delta E_T \quad (1)$$

where *F* is the Faraday constant, ΔE_S is the redox span and ΔE_T is the energy transduced. The redox span equals the difference in the redox potential of the product and substrate redox pools and provides the free energy to pump protons against Δ*P*. The energy transduced equals the product of Δ*P* and the pumping stoichiometry (number of protons pumped per electron) and is the energy required to pump the protons. Since a high Δ*P* is necessary to maintain a high ΔG_{ATP}, and the redox free energy available to complex I and III is limited [6], these proton pumps must operate with a high thermodynamic efficiency ($\Delta E_T/\Delta E_S$), and hence close to equilibrium (small Δ*G*). The normal metrics for enzyme function, k_{cat} and K_M, are measured infinitely far from equilibrium and therefore shed little light on the in-vivo function of the ETC. For instance, the electron flux can change by an order of magnitude between state 4 and state 3 even though the k_{cat} of the complexes, which are measured with saturating substrate and in the absence of

* Corresponding author.
E-mail address: Roger.Springett@kcl.ac.uk (R. Springett).

https://doi.org/10.1016/j.bbabio.2018.11.013
Received 16 February 2018; Received in revised form 4 October 2018; Accepted 7 November 2018
Available online 08 November 2018
0005-2728/

Table 1
K_M (NADH/NAD^+ and UQH_2/UQ) or K_d (Cytc) for the pumping complexes and concentrations of the intermediate redox pools in the matrix (NADH/NAD^+), in the inner membrane (UQH_2/UQ) and in the intermembrane space (Cytc).

Complex	K_M or K_d	Pool	Concentration
I	≈80 μM [10]	NADH/NAD^+	≈3.5 mM [11]
	≈480 μM [10]	UQH_2/UQ	≈12 mM [12]
III	≈600 μM [13]		
	≈9.5 μM [14]	$Cytc^{2+}$/$Cytc^{3+}$	≈700 μM [15]
IV	≈10–30 μM [16,17]		

product and ΔP, is the same. Furthermore, the proton pumping complexes must operate below their k_{cat} to achieve high thermodynamic efficiency and probably do not turnover at k_{cat} even in state 3 because ΔP is not zero [7] and the substrate pools are not fully reduced (the NADH/NAD^+ and Cytc pools are 40–50% and 85–95% oxidized, respectively [8]). Also, the concentrations of the intermediate redox pools are much higher than their K_M or K_d (see Table 1) so that the substrates only become limiting when the intermediate redox pools are at the extremes of their oxidation states. Likewise, complex activities measured with current biochemical assays will poorly reflect how these are functioning in the electron transport chain of living cells since these assays use saturating concentrations of substrate and minimal product, which is supplied to the active site by lysing the inner membrane, hence collapsing ΔP [9]. Under these conditions, the proton pumps operate far from equilibrium (they have a very high redox span and do not transduce energy) and the factors which limit maximal flux will be different from those that determine flux near equilibrium. As such, new metrics are needed to quantify complex function under these physiological conditions.

Close to equilibrium, the electron flux through complex I and III is linear with respect to the ΔG and saturates further from equilibrium [16–18]. In the linear regime, the electron flux, J, measured in units of electrons/second/complex is related to ΔG by:

$$J = -\sigma \Delta G \quad (2)$$

where σ is the constant of proportionality. This constant is independent of the protein level, it is expressed in units of electrons/second/complex/millivolt, and must be large for both complexes I and III to obtain high flux near equilibrium (small ΔG). We have named it the functionality as it represents the ease at which the disequilibrium can drive flux through the individual complex, and therefore could be a good metric of the function of a complex under physiological conditions. Regulation of ETC flux can be achieved by fine tuning the functionality through different subunit composition [18] or post-translational changes such as phosphorylation [19,20] or nitrosylation of complex I [21], and methods to detect these, accurately, need to be in place.

The goal of this paper is to explore the functionality of complex I and III in living cells as a metric of function. Although complex IV operates far from equilibrium and the functionality is not appropriate, we develop a similar metric by quantifying the relative contribution of Cytc and ΔP to turnover. We map out the force-flux relationships of the pumping complexes using oligomycin, to bring the ETC close to equilibrium at low flux, and with increasing concentrations of a protonophore, to increase the electron flux to maximal rates. This is carried out in control cells and cells treated with low concentrations of inhibitors to selectively modify the functionality. We find that the functionality of complex III is very dependent on the redox poise and that both azide and cyanide have very different effects on complex IV. Importantly, we demonstrate that our system allows accurate detection of changes in the functionality of the pumps in living cells and therefore can be used in subsequent studies to investigate the effect of small molecules, mutations or post-translational modifications on the ETC.

2. Materials and methods

2.1. Cell culture

RAW 264.7 mouse macrophage cells were cultured at 37 °C in Wheaton™ Magna-Flex™ spinner flasks in RPMI medium supplemented with 10% heat-inactivated fetal bovine serum, 5 mM D-glucose and penicillin/streptomycin antibiotics, in a 95% air and 5% CO_2 incubator. Cells were spun down at 500*g* for 5 min, and re-suspended at a density of 2×10^7 cells/mL in a custom RPMI media without vitamin supplements to reduce the background auto fluorescence.

2.2. Chamber and oxygen consumption

Studies were performed as described previously [22]. Briefly, cells were placed in a 5 mL measurement chamber, where they were stirred, maintained at 37 °C with a thermoelectric element, and sealed with a plunger. Oxygenation was remotely-controlled and kept constant at a concentration of 100 μM (unless stated otherwise) by passive transfer of oxygen across 80 mm of silicon tubing submerged in the cell suspension. Oxygen tension in the chamber was continuously monitored using an oxygen optode and the O_2 consumption was calculated from the oxygen delivery and the rate of change of the oxygen concentration in the cell suspension.

2.3. Spectroscopy

The spectroscopy system has been described previously [23]. In brief, heme attenuation spectra and NADH fluorescence spectra were measured with two separate CCD-spectrograph systems working in time-multiplexed mode at 50 Hz and contiguous spectra were averaged to give a temporal resolution of 0.5 s. A warm white light emitting diode (LED) was used for the attenuation spectra illumination and a 365 nm UV LED was used for NAD(P)H fluorescence excitation. The spectral fitting algorithms employed a linear combination of model spectra to calculate oxidation changes of the hemes and NAD(P)H as described previously [23]. For heme oxidation changes, the model spectra were b_H, b_L, c_1 hemes of complex III, heme *c* of cytochrome *c*, a_{605}, a_{602} and a_3 spectra from complex IV [24] and a quadratic background to account for any baseline drift with a fitting range 520–630 nm. The NADH model spectra were the fluorescence spectrum of NADH, the fluorescence spectrum of the RPMI medium and a linear background with a fitting range of 410–610 nm.

2.4. Experimental protocol

Fig. 1 in results shows an example of the data collection and protocol for cells inhibited with cyanide. After a brief period of anoxia to fully reduce the hemes and the mitochondrial NAD^+/NADH pool, the oxygen concentration was returned to 100 μM and the cells allowed to stabilize for 8 min before being treated with 3 doses (Fig. 1 arrows I) of either: 3 nM of piericidin, 100 μM of azide or 5 μM cyanide, each separated by 2 min. Control cells were not treated with an inhibitor. Four minutes after the last inhibitor dose, the cells were treated with oligomycin (Fig. 1 arrow O) to inhibit the ATP synthase and bring the ETC close to equilibrium and then with eight 200 nM doses (Fig. 1 arrows B) of the protonophore BAM15 [25] to increase electron flux and oxygen consumption. Studies were then ended with the addition of a high concentration (2 μM) of the protonophore carbonyl cyanide *m*-chlorophenyl hydrazone (CCCP) and 1 mM of the complex II inhibitor 3-nitropropionic acid (3-NPA) to collapse ΔP and inhibit the TCA cycle, respectively, and so to fully oxidize the mitochondrial NADH/NAD^+ pool. Finally, the cells were treated with 1 μM rotonone to fully inhibit complex I and fully oxidize the hemes.

The NAD(P)H fluorescence originates from NADH and NADPH in both the mitochondrial matrix and the cytosol. Both the excitation

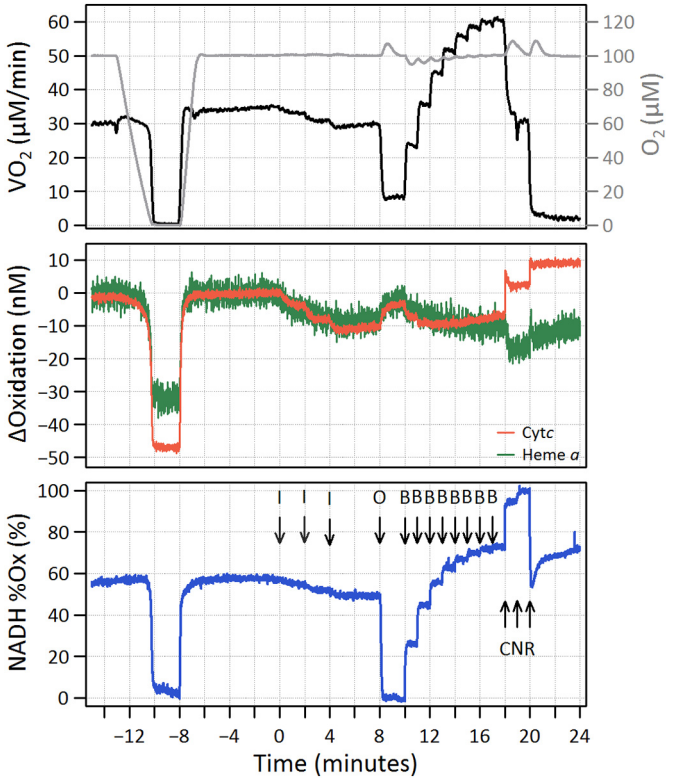

Fig. 1. Example of the protocol and data collection. Graphs show the oxygen concentration (O_2, light grey trace of the upper panel), oxygen consumption (VO_2, black trace of the upper panel), oxidation changes of both Cytc and complex IV heme *a* (middle panel), and the NAD^+/NADH oxidation state, upon the addition of an inhibitor (arrow "I", representing here 5 μM cyanide), 5 μg/mL oligomycin ("O"), 200 nM BAM15 ("B"), 2 μM CCCP ("C"), 1 mM 3-NPA ("N") and 1 μM rotenone ("R").

spectrum and the emission spectrum of NADH and NADPH are identical and the signals cannot be separated spectrally. Likewise, the mitochondrial and cytosolic florescence cannot be separated without using microscopy. Time resolved fluorescence studies have shown that the fluorescence predominantly originates from bound NADH or NADPH which has a longer non-radiative lifetime and so greater fluorescence quantum efficiency [11]. Comparison between the fluorescence signal and the absorption signal, which is equally sensitive to bound and unbound NAD(P)H, are linearly related so that the fluorescence signal from bound NAD(P)H can be used to calculate the oxidation state of the free NAD(P)H pool [11]. In this study, we made the assumption that the anoxia and mitochondrial inhibitors did not affect NADPH and the cytosolic NADH levels so that changes in the fluorescence signal were only due to changes in the mitochondrial NADH levels. With this assumption, the oxidation state of the mitochondrial NADH/NAD^+ was back-calculated from the fully reduced state during the anoxia and the fully oxidized state after 3-NPA and the CCCP at the end of the study. Likewise, The oxidation state and content of the hemes was also back-calculated from the fully reduced state during the anoxia and the fully oxidized states recorded after addition of rotenone at the end of the study to give the content of complex III, Cytc and Complex IV. In studies using the complex IV inhibitors azide and cyanide, heme *a* did not fully oxidize after rotenone and the content of complex IV was calculated from the reduction during the anoxia corrected for the mean baseline oxidation state of heme *a* measured in the untreated cells. The residual oxygen consumption after treatment with rotenone was considered to be the non-mitochondrial in origin and subtracted from the total oxygen consumption to give the mitochondrial oxygen consumption. The mitochondrial oxygen consumption and content was then used to calculate the turnover number of complex III, Cytc and Complex IV, in units of e/CIII/s, e/Cytc/s and O_2/CIV/s, respectively.

2.5. Redox potentials and ΔP

The proton motive force (ΔP) is the sum of the membrane potential ($\Delta\Psi$) and the pH gradient express in millivolts (ΔpH), which is given by $\Delta pH = (RT/F)Ln(10)(pH_m\text{-}pH_c)$ where R is the gas constant, T is the temperature in Kelvin, F is the Faraday constant and pH_m and pH_c are the pH of the matrix and cytosol, respectively. The ΔG of complex I, III and IV, expressed in millivolts (calculate from $\Delta G/F$), is given by:

$$\Delta G_I = -(E_h^{UQ} - E_h^{NADH}) + 2\Delta P$$
$$\Delta G_{III} = -(E_h^{Cytc} - E_h^{UQ}) + \Delta\Psi + 2\Delta pH$$
$$\Delta G_{IV} = -(E_h^{O_2} - E_h^{Cytc}) + \Delta\Psi + \Delta P \quad (3)$$

where E_h^{NADH}, E_h^{UQ}, E_h^{Cytc} and E_h^{O2} are the redox potentials of the NAD^+/NADH, UQ/UQH_2, $Cytc^{3+}$/$Cytc^{2+}$ and O_2/H_2O pools. The term in brackets on the left is the redox span (ΔE_S) and the other terms are energy transduced (ΔE_T). Complex I transfers electrons from the NAD^+/NADH pool to the UQ/UQH_2 pool and pumps 2 protons per electron transferred giving a ΔE_T of 2ΔP. Complex III transfers electrons from the UQ/UQH_2 pool to the Cytc pool and operates by the Q-cycle [26] in which electrons from the oxidation of UQH_2 at the Qo centre (on the cytosolic side of the membrane) are bifurcated such that one electron reduces Cytc and the other reduces a UQ at the Qi centre (matrix side), see [27] for a recent review of complex III. The $\Delta\Psi$ component of ΔE_T is due to the movement of charge across the membrane in the form of an electron from the Qo centre to the Qi centre, the net charge of 2 protons and an electron from the Qo centre to the cytosolic side of the membrane and the uptake of a proton to the Qi centre from the matrix. The $2\Delta pH$ originates from the difference in redox potentials of UQ/UQH_2 at the Qo and Qi centres due to the origin of the protons being from the cytosolic and matrix sides of the membrane, respectively [15]. Complex IV reduces oxygen to water at the binuclear centre (BNC) buried in the protein using electrons from the Cytc pool and protons from the matrix. The ΔP term of ΔE_T is due to the pumping of one proton per electron transferred to the BNC and the $\Delta\Psi$ term is due to the movement of the electron and substrate proton to the BNC against the membrane potential.

A summary of how the parameters are calculated is given in Table 2. The calculation of the $\Delta\Psi$, E_h^{UQ} and ΔpH from the redox poise of complex III has been described previously and the approximations discussed and justified [15,28]. In brief, the membrane potential ($\Delta\Psi$) was calculated assuming the electron transfer from the b_L to the b_H heme of complex III occurs at equilibrium e.g.

$$\Delta G_{b_L \to b_H} = -(E_h^{b_H} - E_h^{b_L}) + \beta\Delta\Psi = 0 \quad (4)$$

where $E_h^{b_H}$ and $E_h^{b_L}$ are the redox potentials of the b_H and b_L hemes, respectively, and β is the fractional dielectric separation of the hemes in the membrane and assumed to be 0.5 [29]. The redox potentials of b_H and b_L were calculated from their measured oxidation states using a redox anticooperativity model [28] with midpoint potentials of +40 and −20 mV, respectively, and an interaction energy of 70 mV [29]. The redox potential of the ubiquinone pool was calculated assuming the transfer of an electron from the b_H heme to the UQ/UQH_2 pool at the Qi centre occurs at equilibrium, e.g.

$$\Delta G_{b_H \to UQ} = -(E_h^{UQ} - E_h^{b_H}) + \alpha\Delta\Psi = 0 \quad (5)$$

where α is the dielectric depth of b_H and assumed to be 0.25 [15]. The pH gradient is calculated with an *in-silico* model of complex III using the measured values of E_h^{Cytc}, E_h^{UQ} and $\Delta\Psi$, assuming the cytosolic pH was 7.0 and then varying the matrix pH until the modeled turnover number matches the measured turnover number [15]. The parameters of the *in-silico* model of complex III are exactly as given previously [15] where their justification and provenance are given in the supporting material.

Table 2
Summary of how the parameters are calculated from the experimental data.

Parameter	Origin
E_h^{Cytc}	Calculated from the measured oxidation state of Cytc using the Nernst equation and E_m = 260 mV (Eq. (6))
E_h^{bH}, E_h^{bL}	Calculated from the measured oxidation states of b_H and b_L using the Nernst equation extended to include the redox anti-cooperativity between the hemes.
E_h^{UQ}	Calculated from the redox potential of b_H assuming equilibrium (Eq. (5))
E_h^{NADH}	Calculated from the measured oxidation state of NADH using the n = 2 Nernst equation and E_m = −320 mV (Eq. (6))
$\Delta\Psi$	Calculated from the difference in redox potentials of b_H and b_L assuming equilibrium (Eq. (4))
ΔpH	Calculated using a turnover model of complex III. The model has E_h^{UQ}, E_h^{Cytc} and $\Delta\Psi$ fixed at the measured values and ΔpH is varied until the modeled turnover matches the experimental turnover.
Cytc *c*, Complex III and IV content	Oxidation change (nM) of the b-hemes (complex III), c-heme (Cyt *c*) or heme *a* (complex IV) between fully oxidized (after inhibitors at end of study) and fully reduced (anoxia).
Turnover number of Cyt *c*, CIII and IV	Complex IV: oxygen consumption (nM/s) divided by complex IV content (nM). Complex III: electron flux (4 × oxygen consumption in nM/s) divided by complex III content (nM). Cyt *c*: electron flux (nM/s) divided by Cyt *c* content (nM)

The model and the methods for calculation $\Delta\Psi$, ΔpH and E_h^{UQ} have been further discussed [22].

The Nernst equations for the redox potentials are:

$$E_h^{NADH} = E_m^{NADH} + \frac{RT}{2F}\mathrm{Ln}\left(\frac{[NAD^+][H^+]}{[NADH]}\right)$$
$$E_h^{UQ} = E_m^{UQ} + \frac{RT}{2F}\mathrm{Ln}\left(\frac{[UQ][H^+]^2}{[UQH_2]}\right)$$
$$E_h^{Cytc} = E_m^{Cytc} + \frac{RT}{F}\mathrm{Ln}\left(\frac{[Cytc^{3+}]}{[Cytc^{2+}]}\right)$$
$$E_h^{O_2} = E_m^{O_2} + \frac{RT}{4F}\mathrm{Ln}\left(\frac{[O_2][H^+]^4}{[H_2O]}\right) \quad (6)$$

where E_m is the respective midpoint potential under standard conditions, the proton concentrations are those of the matrix and the square brackets denote concentration of the metabolite as a fraction of the concentration under standard conditions. Standard conditions are defined as metabolites at a concentration of 1 M, an oxygen concentration of 957 µM (100% O_2 in saline media), [H_2O] = 1.0, pH 7.0 and 37 °C. The matrix pH was calculated from ΔpH assuming the cytosol was at pH 7.0. The redox potential of the Cytc and NADH pools were measured from the measured oxidation states using an E_m of 260 and −320 mV, respectively, and the O_2 assuming the oxygen concentration was 100 µM (see Fig. 1) and an E_m of 815 mV [30]. The oxidation state of the UQ/UQH_2 pool was calculated from the redox potential assuming an E_m of 90 mV, as used in the *in-silico* model.

3. Results

3.1. Kinetic and thermodynamic parameters of the electron transport chain

Mitochondrial function in living cells is adapted to the metabolic requirements of tissues, and its characterisation is essential to understand the basic physiology of cells. We used multi-wavelength spectroscopy to quantify mitochondrial function in RAW cells. Experiments started with a brief period of anoxia and ended with the addition of a high concentration of mitochondrial inhibitors (Fig. 1. CCCP, arrow labelled 'C'; 3-NPA, arrow 'N', and Rotenone, arrow 'R'. See 2.4 Experimental protocol) to fully oxidize the electron transport chain. This approach allowed us to infer on important kinetic and thermodynamic parameters of the proton pumping complexes and Cytc, such as the content of the hemes of complex III, Cytc and complex IV, and therefore the content of complex III, Cytc and complex IV (Table 3), as well as the oxidation state and redox potential of the intermediate redox pools at baseline (Table 4). Furthermore, using developed algorithms, we recorded that under normal conditions (untreated cells), the baseline $\Delta\Psi$ was 157 ± 3 mV, ΔpH was 30 ± 2 mV, ΔP was ≈187 ± 2 mV and oxygen consumption was 34 ± 7 µM / min (mean ± SD, n = 6).

3.2. Effects of mitochondrial inhibitors on the electron flux and redox poise of the ETC

To investigate the effect of known mitochondrial inhibitors on the electron flux and redox poise, cells were treated with three equal doses of either 3 nM piericidin to inhibit complex I, or 100 µM azide/5 µM cyanide to inhibit complex IV, as illustrated in Fig. 1 (Fig. 1: arrow labelled 'I' for the addition of inhibitors at 0, 2 and 4 min. See 2.4 Experimental protocol).

Inhibiting complex I with piericidin led to a ~5 mV reduction of the NADH pool, as expected since NAD + /NADH is upstream of the site of inhibition (complex I), also to an oxidation of the UQ and Cytc pools, as both are downstream of it, together with a decrease in oxygen consumption (Fig. 2a, b and c - blue bars). Likewise, inhibiting complex IV with azide led to a reduction of the NADH, UQ and Cytc pools upstream of the site of inhibition and also to a decrease in oxygen consumption (Fig. 2a, b and c - light green). Cyanide, another inhibitor of complex IV, similarly led to a reduction of the Cytc pool and a decrease in oxygen consumption, however no changes in the redox potentials of the NADH and UQ pools were recorded (Fig. 2a, b and c - dark green bars); the oxidation state of the NADH pool changed from 61% to 55% oxidized on addition of cyanide but this reduction was countered almost perfectly by the acidification of the matrix. Similarly, the oxidation state of the UQ pool, calculated from its redox potential and matrix pH, changed from 58 to 42% oxidized.

Treatment with these inhibitors also impacted on ΔP (Fig. 2d, e and f). Piericidin led to a slight but non-significant decrease in ΔP due to a small decrease in $\Delta\Psi$ whereas treatment with azide or cyanide significantly decreased ΔP due to either a decrease in $\Delta\Psi$ at constant ΔpH for azide or decrease in ΔpH at constant $\Delta\Psi$ for cyanide. Plotting oxygen consumption as a function of ΔP (Fig. 2h) showed that the ETC respond very differently to piericidin and to the complex IV inhibitors: piericidin resulted in a marked decrease in oxygen consumption with very little change in ΔP whereas both azide and cyanide elicited very similar responses with decreases in oxygen consumption and ΔP, albeit from a slightly different baseline.

3.3. Effects of mitochondrial inhibitors on the functionality of complexes complex I and III

The functionality is the ease at which the disequilibrium drives electron transport and proton pumping of a complex. To investigate whether the functionality of the complex I and III can be used as an accurate metric, cells were treated with oligomycin (Fig. 1 arrow "O") to inhibit the ATP synthase and increase ΔP, and then titrated with 8 low doses of a protonophore (200 nM BAM15, Fig. 1, arrow "U") to decrease ΔP. This protocol allows the examination of the response of the ETC to changes in ΔP in the presence or absence of inhibitors and the mapping of the force-flux relationships for complex I, III, I + III (Fig. 3) and IV (Fig. 6e).

Table 3
Content, turnover number and components of the free energy change of the proton pumping complexes and Cytc, under physiological conditions in RAW 264,7 mouse macrophages.

	Complex I	Complex III	Cytc	Complex IV
Content	n.a.	15.0 ± 2.6 nM	69.7 ± 18.1 nM	46.2 ± 8.1 nM
Turnover number	n.a.	138 ± 10 e/s	30 ± 4 e/s	11.2 ± 0.8 O_2/s
ΔG	−26 ± 5 mV	−13 ± 1 mV	n.a.	−127 ± 7 mV
ΔE_S	400 ± 3 mV	230 ± 3 mV	n.a.	471 ± 5 mV
ΔE_T	375 ± 4 mV	217 ± 3 mV	n.a.	345 ± 5 mV
Efficiency[a]	93.6 ± 1.2%	94.3 ± 0.6%	n.a.	73.1 ± 1.4%

n.a. = not applicable. Value are presented as mean ± SD (n = 6).
[a] The thermodynamic efficiency is given by $\Delta E_T/\Delta E_S$.

Table 4
Oxidation states (% oxidized) and redox potential (mV) of the intermediate redox pools under physiological conditions in RAW 264,7 mouse macrophages.

	NAD^+/NADH	UQ/UQH_2	Cytc
Oxidation state	55 ± 5	65 ± 3	81 ± 2
Redox potential	−332 ± 3	68 ± 2	299 ± 4

Values are presented as mean ± SD (n = 6).

Regarding complex I, its turnover number cannot be directly calculated because it is not possible to separate the contribution of electron flux from both complex I and complex II to the oxygen consumption, and it is not possible to quantitate the content of complex I because this enzyme does not contain hemes. Instead, we use complex III turnover number as a surrogate for complex I turnover number. The relative content of complex I and complex III should not change during these brief studies and, assuming that electron flux originates from the oxidation of glucose via the malate-aspartate shuttle and the TCA cycle, the electron flux through complex I and II should be in the ratio of 5:1. As shown in Fig. 3a and, as expected for a reversible enzyme, the turnover number of complex I was linear with ΔG close to equilibrium and saturated far from equilibrium in both untreated and treated cells. Since the oxidation state of NADH after addition of oligomycin was near zero (Fig. 1), the NADH redox potential, the redox span and the change in free energy of complex I could not be calculated for this point. Four linear regressions were then fitted to the linear portion of the curves (first three data points) and, when extrapolated back to the x-axis, the regression lines crossed the origin at −0.2 ± 3.6, 5.7 ± 11.9, 11.8 ± 9.1 and −4.2 ± 3.5 for the untreated, piericidin, azide and cyanide groups respectively (mean ± SD, n = 6). As expected, 9 nM of piericidin (complex I inhibitor) significantly decreased both the functionality of complex I, as represented by the gradient of the linear regression, and the maximal flux when compared to untreated cells, whereas cyanide (complex IV inhibitor) did not cause any change.

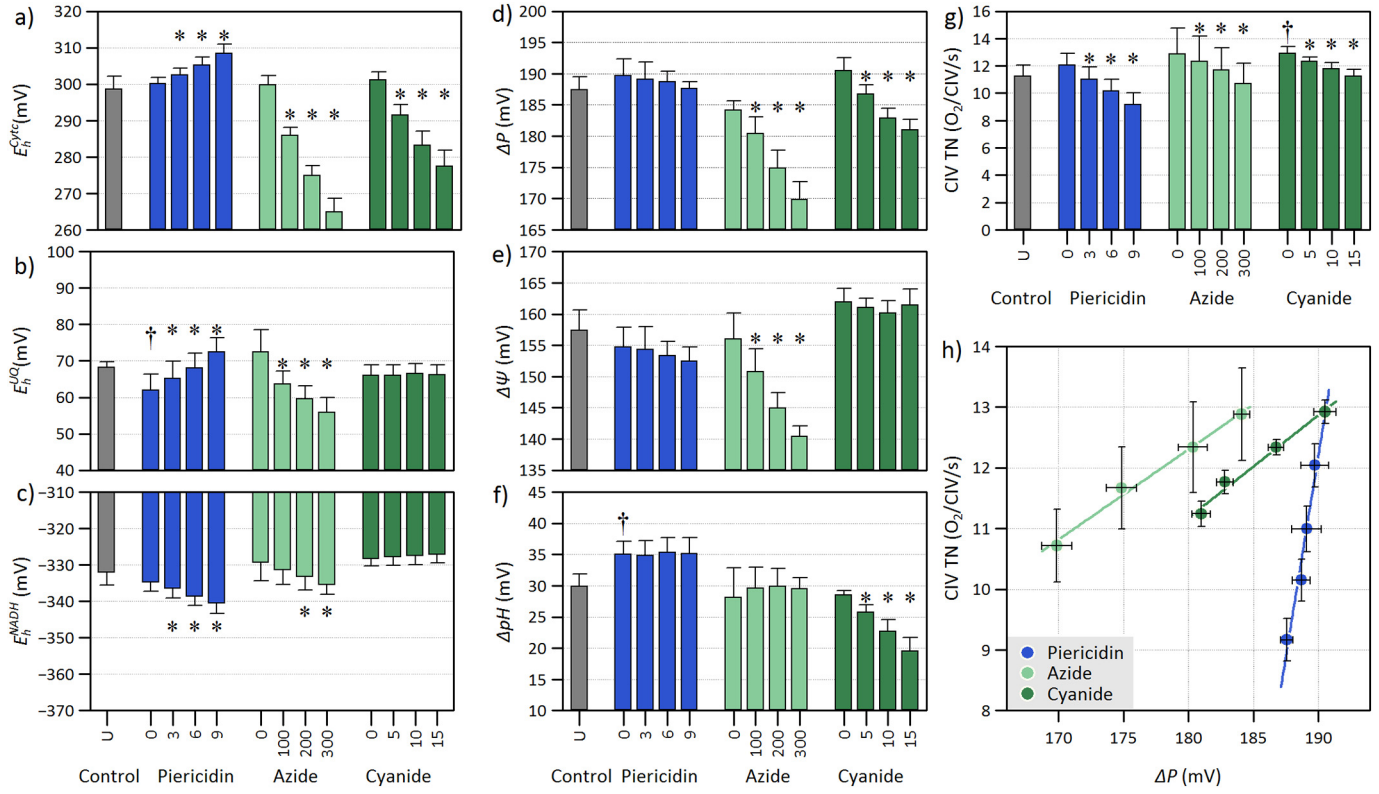

Fig. 2. Redox poise and oxygen consumption of the electron transport chain when treated with complex I or complex IV inhibitors. Graphs show the redox potentials of a) Cytc (E_h^{Cytc}), b) ubiquinone (E_h^{UQ}) and c) NADH (E_h^{NADH}), the d) proton motive force (ΔP), e) mitochondrial membrane potential ($\Delta\Psi$), f) pH gradient (ΔpH) and g) complex IV turnover of cells, following the addition of 3–9 nM of piericidin (complex I inhibitor, blue bars bars), 100–300 μM azide or 5–15 μM of cyanide (complex IV inhibitors, light and darker green, respectively). Graph h) illustrates oxygen consumption as a function of ΔP. Results are expressed as mean ± SD (n = 6) except for h) which is mean ± SE (n = 6). †$p < 0.01$ unpaired *t*-test baseline from control, *$p < 0.01$ paired *t*-test inhibitor from baseline.

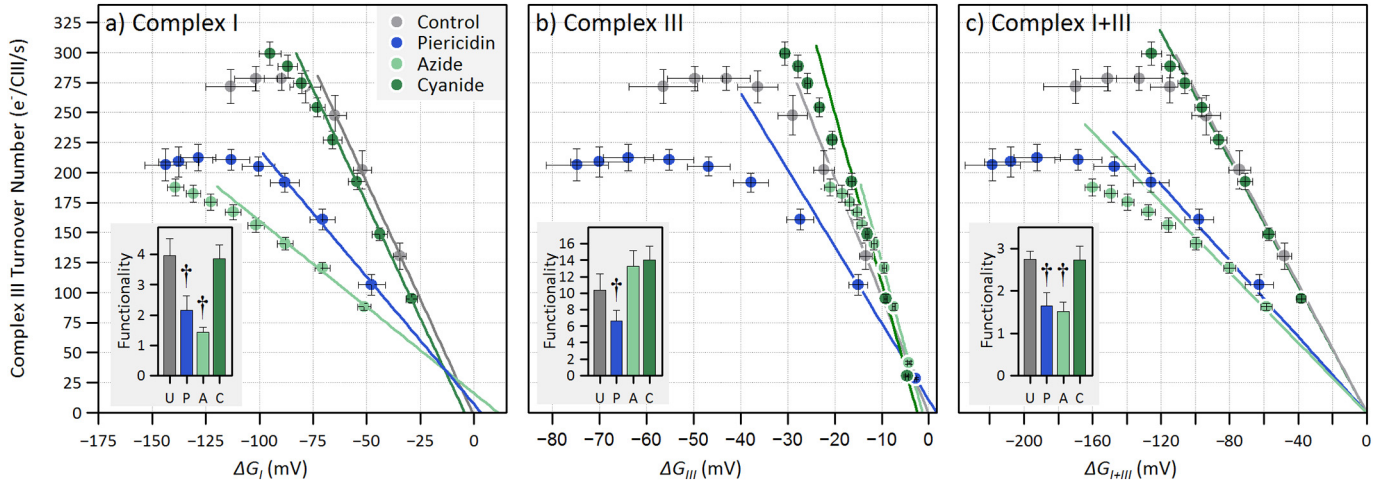

Fig. 3. Functionality of complex I, complex III and the span from NADH to Cyt*c* (complex I + III). Plots map the relationship between force and flux of electron through a) complex I, b) complex III and c) from NADH to Cyt*c*, at the different time points of the BAM15 titration. The data points are expressed as mean ± SE (n = 6) and the lines are regression lines to the linear region (first three points for complex I and the first two points for complex II and complex I + III). The regression line for complex I + III has been restricted to pass through the origin. Insets are the functionality in units of e/CIII/s/mV and expressed as mean ± SD (n = 6) and † indicates a significant difference from control (unpaired *t*-test, $p < 0.01$).

Surprisingly, the well described complex IV inhibitor azide ([30,31]) had a significantly greater effect on complex I functionality than piericidin although the flux did not plateau over this range of ΔG.

The linear region of the force-flux relationship of complex III (Fig. 3b) was smaller than that of complex I and so regression lines were fitted to the first two data points. These lines should pass precisely through the origin because the ΔG for complex III is calculated from the *in-silico* model. However, the model has a precision of only ≈1 mV and the curves are non-linear even over this restricted range resulting in a small deviation of the extrapolated line to the origin. When compared to the untreated cells, piericidin significantly decreased the functionality of complex III while complex IV inhibitors slightly increased its functionality. The change with piericidin is surprising: although piericidin is a ubiquinone analogue, it only inhibits complex III at micromolar concentrations and not at the nanomolar concentration used here [31].

Combining complexes I and III gives a redox span from NADH to Cyt*c* that is independent of ubiquinone and so, independent of errors in the measurement of the ubiquinone redox potential. Again, due to the limited region of linearity and absence of the point at lowest flux, the regression lines were fitted to the first two points and constrained to pass through the origin (Fig. 3c). As visible, the functionality of complex I + III did not change upon treatment with cyanide when compared to untreated cells, whereas it was significantly lower with piericidin and azide. These results suggest that the lower functionality of complex I with azide does not result from errors in the measurement of the ubiquinone pool.

3.4. Components of the redox poise of the ETC upon mitochondrial inhibition

In order to get a greater understanding of how the redox poise and components of ΔP contribute to the ΔG of complex I and III, we plotted these parameters as a function of electron flux during the BAM15 titration (Fig. 4). Regression lines to the first few data points are shown as a guide to the eye and each panel is shown on the same scale so the relative change of each component can be directly compared.

In untreated cells, the redox potential of Cyt*c* (Fig. 4a) was independent of electron flux until high flux was reached, and then oxidized as flux became maximal. The upstream inhibitor piericidin led to an oxidation relative to untreated cells at all fluxes and the downstream inhibitors cyanide and azide led to a reduction, with 300 μM of azide having a greater effect than 15 μM of cyanide. The ubiquinone pool (Fig. 4b) oxidized as the electron flux increased in untreated cells, with the oxidation rate rising markedly as flux became maximal. The relationship was unchanged after cyanide treatment but both piericidin and azide led to an oxidation and reduction of the ubiquinone pool, respectively, when compared to control. Finally, the NADH pool (Fig. 4c) also oxidized with increasing electron flux but barely changed upon treatment with the inhibitors.

Both the $\Delta\Psi$ and ΔpH decreased with increasing electron flux (Fig. 4e and f), as expected, with the changes in $\Delta\Psi$ being much larger than in ΔpH. Azide inhibition caused the largest fall in $\Delta\Psi$ whereas cyanide had little effect on $\Delta\Psi$, when compared to the control. In contrast, cyanide created larger changes in ΔpH with electron flux when compared to the very similar responses recorded in control cells and both piericidin and azide treated cells. For both complex I and complex III the redox span (ΔE_S) decreased with increasing electron flux and the increase in turnover numbers were driven by the greater decrease in transduced energy (ΔE_T) (Fig. 4g). When compared to untreated cells, piericidin increased the redox span of complex I whereas azide and cyanide decreased it.

3.5. The redox poise affects the functionality of complex III

The *in-silico* model of complex III turnover was used to explore the effect of the redox poise on the functionality. Complex III was first poised at equilibrium with $E_h^{Cytc} = 300\,mV + \Delta E_h$, $E_h^{UQ} = 60\,mV + \Delta E_h$, $\Delta\Psi = 190\,mV$ and $\Delta pH = 25\,mV$ where ΔE_h can be used to vary the poise at constant redox span and $\Delta E_h = 0\,mV$ approximates the conditions found in the cells at zero flux (Fig. 5). Complex III was then driven in the forward direction by decreasing $\Delta\Psi$ or ΔpH, or by reducing E_h^{UQ} or oxidizing E_h^{Cytc} and the turnover number was plotted as a function of ΔG (Fig. 5) at three different redox poises ($\Delta E_h = -10$, $+10$ or $+30\,mV$ in Fig. 5a, b and c, respectively). At each redox poise, the turnover was independent of the method of generating ΔG and linear with respect to ΔG close to equilibrium (disequilibrium < 10 mV) such that the gradient (functionality) was independent on the method of generating the disequilibrium. Further from equilibrium (disequilibrium > 10 mV), the curves diverged, the turnover became non-linear with respect to ΔG and dependent on the method of generating the disequilibrium. Although the functionality was independent of the mechanism of generating the disequilibrium, the functionality did depend on the redox poise with a more oxidized

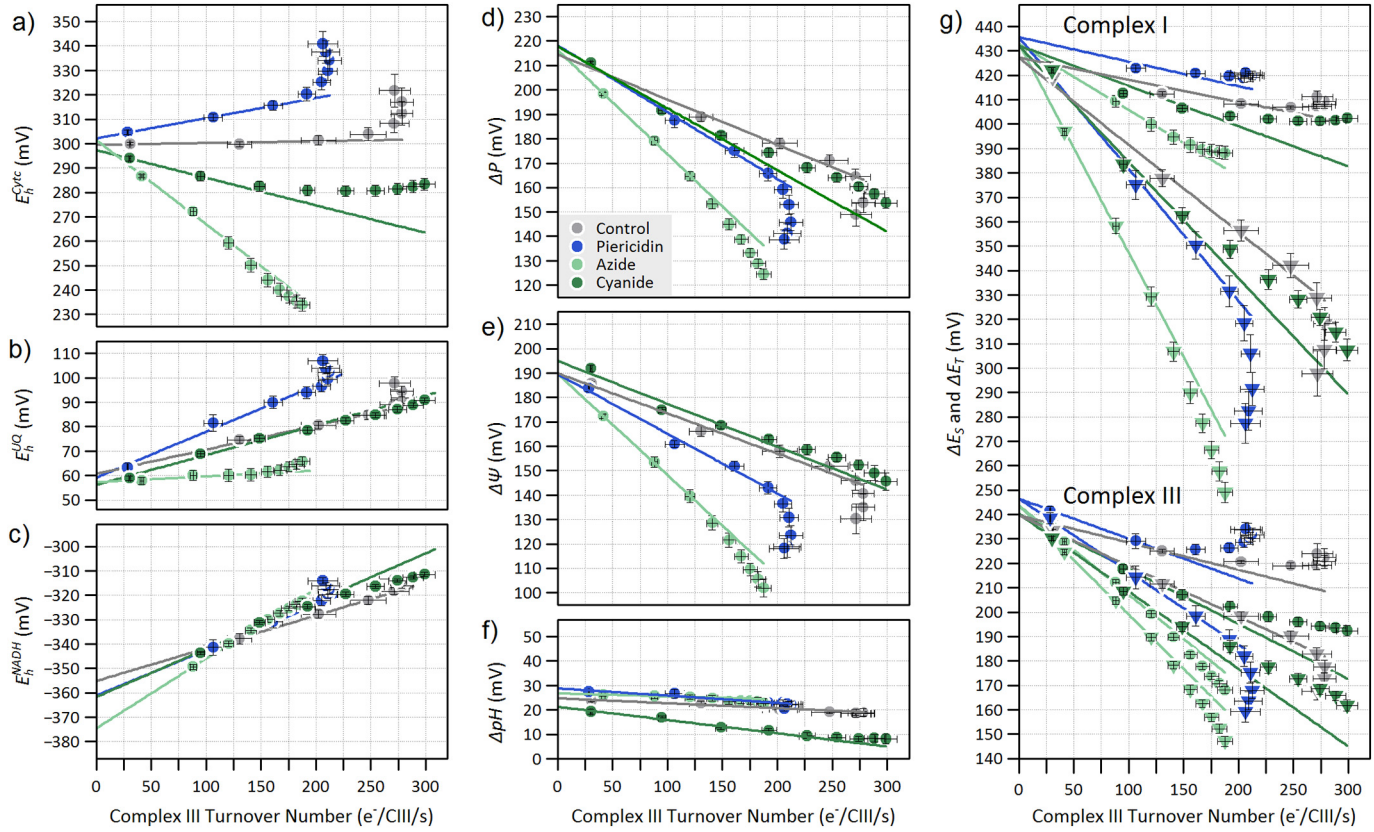

Fig. 4. Redox poise, $\Delta\Psi$ and ΔpH as a function of complex turnover during the BAM15 titration. Graphs plot the redox potentials of a) Cytc (E_h^{Cytc}), b) ubiquinone (E_h^{UQ}) and c) NADH (E_h^{NADH}), the d) proton motive force (ΔP), e) mitochondrial membrane potential ($\Delta\Psi$), f) pH gradient (ΔpH), and g) both redox span (ΔE_S) and energy transduced (ΔE_T) of complexes I and III, as a function of electron flux following the addition 9 nM of piericidin (blue), 300 μM azide or 15 μM of cyanide (light and darker green, respectively). The lines are regressions lines to the linear region and included as a guide to the eye. Each panel is shown on the same scale so that changes can be directly compared. In g), the ΔE_S (upper data points represented as circles) and the ΔE_T (lower data points represented as triangles) regression lines for each treatment have been restricted to cross the Y-axis are the same point. Data is expressed as mean ± SE (n = 6).

poise giving a lower functionality. Plotting the functionality against redox poise (Fig. 5c, inset) shows that the maximum functionality occurs when ΔE_h is −4 mV, very close to the redox poise found in untreated cells extrapolated to zero turnover. This suggests that the small increase and decrease in functionality with complex IV and complex I inhibitors, respectively, is due to a more reduced and oxidized redox poise, respectively, rather than binding and affecting complex III directly.

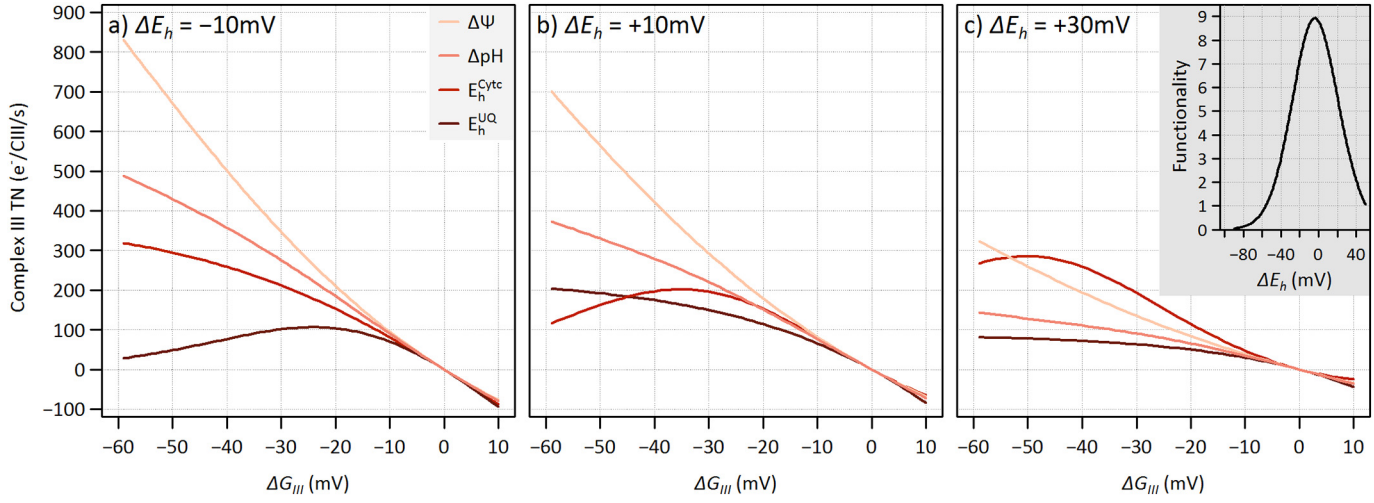

Fig. 5. Modelling the dependence of complex III functionality on redox poise. The model of complex III turnover was poised at equilibrium with E_h^{Cytc} = 300 mV + ΔE_h, E_h^{UQ} = 60 mV + ΔE_h, $\Delta\Psi$ = 190 mV and ΔpH = 25 mV and then flux initiated by either varying $\Delta\Psi$, ΔpH, E_h^{Cytc} or E_h^{UQ}. The insert of c) shows the functionality (e/CIII/s/mV) as a function of ΔE_h. This was calculated from the flux of the model at a ΔG of −1 mV from the equilibrium poise as ΔE_h was varied.

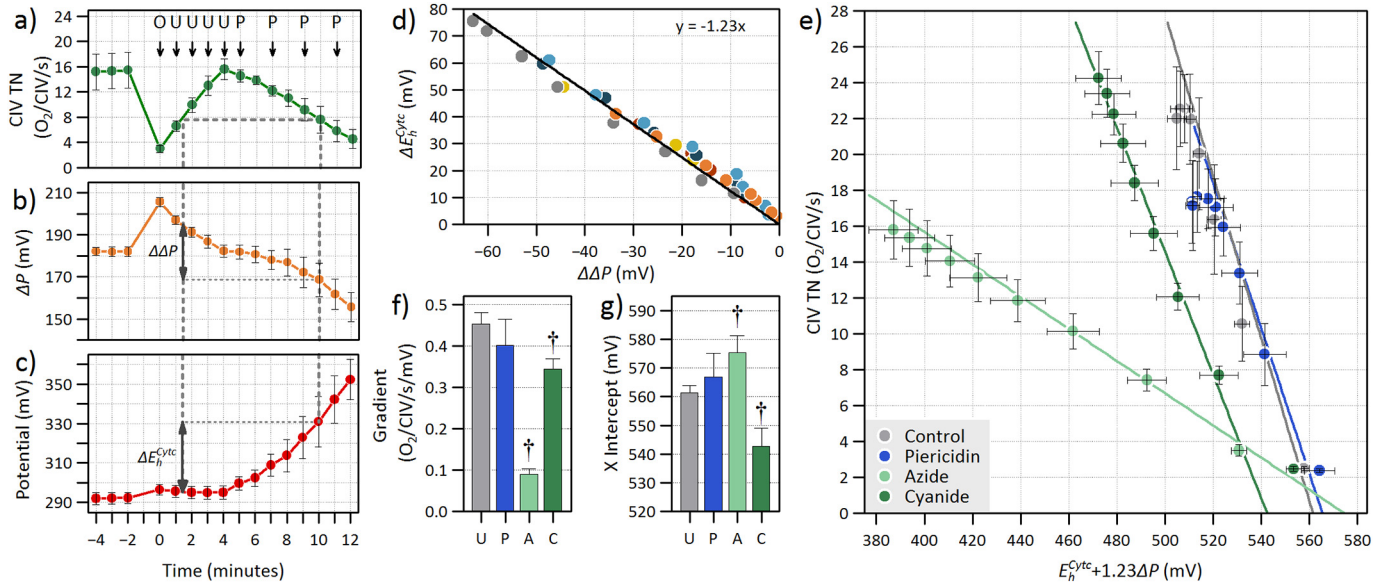

Fig. 6. Determination of a force-flux relationship of complex IV. Graph a–c) illustrates the null-point study performed to determine changes in ΔP ($\Delta\Delta P$) and the E_h^{Cytc} (ΔE_h^{Cytc}) that result in constant complex IV turnover. Cells were sequentially treated with oligomycin (O), 4 doses of 100 nM of BAM15 (U) and 4 doses of 7.5 nM piericidin (P). The yellow and red lines show how $\Delta\Delta P$ and ΔE_h^{Cytc} were calculated, respectively, for each data point in the piericidin titration. d) Relationship between $\Delta\Delta P$ and ΔE_h^{Cytc} for the individual points from 6 studies. The line is a linear regression restricted to pass through the origin and has a gradient of 1.23. e) Force flux relationship for complex IV using $E_h^{Cytc} + 1.23\Delta P$ as the driving force. f and g) gradient and x-intercept of the individual studies expressed as mean ± SD (n = 6) and † indicates a significant difference from untreated (unpaired *t*-test, $p < 0.01$).

3.6. Measuring the functionality of complex IV

As opposed to complex I and III, complex IV operates far from equilibrium (Table 3) and thus functionality is not an appropriate metric. The turnover of complex IV depends on ΔP and E_h^{Cytc} such that a decrease in ΔP or a reduction in Cyt*c* increases turnover. To address the lack of a measure, we developed a protocol to quantitate the dependence of turnover on ΔP and E_h^{Cytc}. Ideally, the dependence on each would be determined by fixing one and measuring the turnover while the other parameter is varied. Since this is not possible to perform in the living cells, the relative contribution of each was determined by a null point study in which the decrease in ΔP necessary to maintain constant turnover in the presence of an oxidation in Cyt*c* was determined. The methodology is shown in Fig. 6a–c. The cells were first treated with oligomycin, which decreased oxygen consumption and increased ΔP. They were then treated with 4 doses of 100 nM BAM15 which increased complex IV turnover, decreased ΔP and resulted in a small oxidation of Cyt*c*. Finally, they were treated with 4 doses of 7.5 nM piericidin which decreased complex IV turnover, decreased ΔP and oxidized Cyt*c*. The value of ΔP and E_h^{Cytc} was interpolated during the additions of BAM15 to give the same turnover number as after each dose of piericidin (Fig. 6a–c, blue lines). This gave 8 pairs of the change in ΔP ($\Delta\Delta P$) and the change in Cyt*c* (ΔE_h^{Cytc}) for each experiment which, in combination, do not change the turnover number. These experiments were repeated 6 times and the 48 pairs of $\Delta\Delta P$ and ΔE_h^{Cytc} were plotted where a linear response was observed (Fig. 6d). A linear regression restricted to pass through the origin gave a gradient of 1.23, meaning that a 10 mV decrease in ΔP can be countered by a 12.3 mV oxidation in Cyt*c*; this implies that the turnover of complex IV is a function of $\Delta E_h^{Cytc} + 1.23\Delta P$ and that this parameter is the driving force for complex IV turnover.

Surprisingly, when complex IV turnover number was plotted as a function of $E_h^{Cytc} + 1.23\Delta P$ for the oligomycin and BAM15 titration data in untreated cells, a linear relationship was found (Fig. 6e); the regression's gradient was 0.417 ± 0.068 O_2/s/CIV/mV and the x-axis intercept was ≈563 mV. As expected, this relationship was not affected by pre-treating the cells with 9 nM of piericidin (complex I inhibitor) because the decrease in complex IV turnover is due to the consequent downstream oxidation of Cyt*c* rather than a direct inhibition of complex IV. Also, as expected, both azide and cyanide inhibited complex IV so that, for a given driving force, the turnover was lower. Pre-treatment with 300 μM azide did not affect the x-axis intercept but decreased the gradient by ≈4.8 fold to a value of 0.087 ± 0.015, consistent with a 79% of complex IV completely inhibited at this concentration and leaving the remaining 21% functioning normally. In contrast, cyanide did not affect the gradient of the response, except at the lowest turnover where the relationship deviated from linearity, but rather decreased the crossing point by ≈25 mV to ≈540 mV.

4. Discussion

The accurate characterisation of the mitochondrial respiratory chain is challenging, requiring in many developed protocols the lysis of cells and isolation of mitochondria. The present work describes a new approach for investigating ETC flux and its regulation in living cells under physiological conditions. We have characterised RAW cells in kinetic and thermodynamic dimensions and showed the importance of this accurate quantification since inhibition of the same complex may lead to different downstream effects (azide vs cyanide). Also, we introduce a new metric - the functionality - which reflects how well complexes I, III and IV are working and we believe it can be used in future studies to underpin (patho)physiological mechanisms underlying the regulation of mitochondrial function.

4.1. Background for the equilibrium model

Standard biochemical assays to measure the activities of the mitochondrial complexes are non-physiological since ΔP is collapsed, substrate is supplied at high concentration and products are minimal, making the complexes operate far from equilibrium. These assays will therefore poorly reflect the actual flux in-vivo and will provide little information of how the ETC functions as an integrated system. In the present study, we measured the redox potential of the donor and acceptor pools of complexes I, III and IV, along with both components of

ΔP, so that we can characterize their function as if they were isolated while they still operate in their authentic environment and as part of the ETC. Our system allows the accurate investigation of the ETC in living cells and can precisely detect changes in the functionality of the pumps - as discussed in the subsequent sections.

In these studies, E_h^{UQ} and $\Delta\Psi$ were calculated from the redox poise of the b-hemes of complex III assuming equilibrium and, using these parameters together with E_h^{Cytc}, the ΔpH was estimated by matching the turnover number of an *in-silico* model of complex III to the measured turnover number [15,28]. Once ΔpH has been determined, the calculation of ΔP, ΔG_I, ΔG_{III} and the driving force for complex IV is straightforward and the functionalities can be measured. However, the accuracy of these measurements is predicated on the accuracy of calculating $\Delta\Psi$ and ΔpH.

Complex III is able to precisely bifurcate the electrons into the high and low potential chains but the mechanism of precise bifurcation is not known [32,33]. The first stochastic kinetic model, developed by the Mazat group [32,34], addressed the precise bifurcation mechanism by including both the bifurcation elementary reactions (first electron passed to the Rieske centre and the second electron transferred to b_L) and the short circuit elementary reactions (first electron passed to b_L and the second electron passed to the Rieske centre). For simplicity, these elementary reactions combined the electron transfer and the proton transfer, and estimated the rate constants using the Dutton ruler for electron transfer thus neglecting the contribution of the proton transfer. As predicted by Osyczka et al. [35], this model displayed considerable short circuiting when the model was inhibited by antimycin and b_L became reduced. We took this model and included the redox anti-cooperativity between b_H and b_L and the effects of $\Delta\Psi$ on the rate constants of the electrogenic reactions [15]. However, contrary to the enzyme, the model showed substantial short circuiting under in-vivo conditions. To prevent the short circuiting, we artificially constrained the model to precisely bifurcate by omitting the short circuit elementary reactions. Despite these simplifications, the present model does reproduce the precise bifurcation observed, and therefore allows us to estimate the contribution of ΔpH in determining flux. It is therefore serviceable in the context of the present paper. A more complete model should separate each ubiquinol oxidation into an electron transfer elementary reaction and a proton transfer elementary reaction with the result that the overall rate of ubiquinol oxidation will be highly dependent on the role of the proton (see [36]). The *in-silico* model of Victoria et al. [37] reproduced the experimental kinetics of bifurcation by inclusion of a movement of the intermediate semiquinone closer to b_L to enhance the electron transfer rate constants. They suggested that coulombic repulsion between the anionic semiubiquinone and reduced b_L could prevent one of the short circuit reactions, but this was hypothesis was not tested in their *in-silico* model. More recent work from the same group [38] has suggested other intermediate states that might be involved in the mechanism of precise bifurcation outlining possible scenarios for further improvement. Currently no *in-silico* model is able to reproduce the precise bifurcation naturally without the imposition of artificial constraints.

The parameters used to calculate $\Delta\Psi$ have been taken from direct measurements [29] and have not been adjusted to give reasonable values of $\Delta\Psi$ [15,28]. The parameters of the *in-silico* model of complex III are described and justified in the supporting data of [15] and, likewise, have not been adjusted to give a reasonable value of ΔpH. The observation that the force-flux relationship of complex I can be extrapolated to the origin with good accuracy (in both untreated and treated cells) provides strong evidence that ΔP and ΔG_I have been correctly calculated. Such evidence has not been provided in other studies in isolated mitochondria using the functionality as a metric [39,40].

The linearity between flux and ΔG close to equilibrium has a rigorous derivation in a near-equilibrium thermodynamic analysis and can be illustrated with the reversible Michaelis Menton reaction $E + S \leftrightarrow ES \leftrightarrow EP \leftrightarrow E + P$, where E is an enzyme, S is the substrate and P is the product. The overall reaction, $S \leftrightarrow P$ is made up of 3 individual elementary/micro reactions, $E + S \leftrightarrow ES$, $ES \leftrightarrow EP$ and $EP \leftrightarrow E + P$, each with a forward and reverse rate constant. The ΔG of the overall reaction is equal to the sum of the individual ΔG's and, at equilibrium, the ΔG of the overall reaction and of each micro reaction is zero. When the overall reaction is displaced from equilibrium, all the individual ΔG'*s* must adapt and be displaced from equilibrium to allow equal metabolic flux through each micro reaction; for instance, when the product concentration is decreased from the equilibrium position to initiate net forward flux, the ΔG of the $E + S \leftrightarrow ES$ and $ES \leftrightarrow EP$ micro reactions must become negative to generate flux through these steps. The flux through a micro reaction is linear with respect to its ΔG when the ΔG is much smaller than the thermal energy [28,35], which is 26.7 mV at 37 °C. This has several consequences: the flux and ΔG of the overall reaction will be linear until the ΔG of at least one micro reaction is no longer small compared to the thermal energy. Also, the gradient of this linear region will be independent of the mechanism by which the disequilibrium is created but will be dependent on the poise of the equilibrium (Fig. 5). The proton pumps of the ETC are much more complex than the simple Michaelis Menton scheme with many micro reactions and a branching network rather than a simple linear network, but the principles still hold. The larger number of micro reactions in complex enzymes (see [36,37]) means that the linear region can extend to a larger overall ΔG before one of the individual ΔG is no longer small compared with the thermal energy. Another consequence of the linearity of flux close to equilibrium is that enzymes that function close to equilibrium, such as complex I, complex III, the ATP synthase and the phosphate uniporter, must be reversible because the force-flux relationship will cross the origin with a large gradient (Fig. 5), although the maximal reverse flux is not necessarily as large as the maximal forward flux. In fact, high thermodynamic efficiency and reversibility go hand in hand.

4.2. Complex III functionality

In the present work we describe the functionality as the gradient of the force-flux relationship in the linear region and, although the gradient should be independent of the mechanism creating the disequilibrium, it can depend on the poise of the complex at equilibrium. We found that piericidin, a ubiquinone analogue and potent complex I inhibitor, decreased the functionality of complex III even though it does not inhibit isolated complex III at these concentrations ($I_{50} \approx 10\,\mu M$) [31]. Using our *in-silico* model of complex III, which is not affected by piericidin, we found that the functionality of complex III has a maximum at a redox poise slightly more reduced (−4 mV) than that found in untreated cells and that the functionality was quite dependent on the redox poise. This is understandable because, when the UQ/UQH_2 pool is very oxidized, there is little ubiquinol for oxidation at the Qo centre, and when the pool is highly reduced there is little ubiquinone available for reduction at the Qi centre. In both cases the turnover and functionality is very low. This dependency could explain the decrease in complex III functionality with piericidin and the small increase with the complex IV inhibitors because piericidin causes a substantial oxidation of the UQ/UQH_2 and Cytc pools due to its effect on complex I and the complex IV inhibitors cause a smaller reduction in these pools. We conclude that changes in the functionality of complex III cannot be used to determine whether small molecules, mutations or post-translational changes affect the function of complex III without taking the redox poise into account.

4.3. Complex I functionality

Complex I is a much larger and more complicated enzyme with many more micro reactions and, as could be predicted, the linear region of the force-flux relationship is larger than for complex III. As expected, cyanide did not change the functionality of complex I when compared

to untreated cells and piericidin decreased both the functionality and the maximal flux consistent with the inhibition of complex I. Surprisingly, 300 μM of azide also reduced the functionality of complex I, and to a greater extent than 9 nM of piericidin.

Azide is best known as an inhibitor of complex IV [41], but also inhibits the ATP synthase [42] and acts as a weak uncoupler [43], which can be seen in Fig. 4d as a concurrent decrease in ΔP and an increase in the electron flux after addition of oligomycin in the azide treated cells when compared to the other cells. As far as we are aware, there are no reports of azide inhibiting complex I or complex III, and azide does not inhibit the isolated complex I (in the absence of ΔP) at this concentration and has only an 8% inhibition at 15 mM (Justin Fedor, private communication). If azide did inhibit complex III then this could affect the calculation of $\Delta\Psi$, ΔpH and E_h^{UQ} leading to an error in the calculated force-flux relationship. However, this is unlikely to be the case because the force-flux relationship of complex I and complex I + III pass through the origin with good accuracy and, similarly, the force-flux relationship of complex IV with and without azide crosses the x-axis at approximately the same value. Also, it is unlikely that such a large effect is caused by a change in the redox poise because the NADH/NAD^+ pool is only slightly more reduced at equilibrium while the UQ/UQH_2 pool is barely changed. While the gradient of the force-flux relationship for azide is smaller than for piericidin, azide does not cause the relationship to plateau as it does for piericidin in this range of disequilibrium (Fig. 3a), and flux still responds to decreases in ΔP (Fig. 4d). It therefore remains possible that complex I flux might increase and reach the same maximum level of the uninhibited enzyme as ΔP decreases to zero and ΔG becomes very large. If this is the case, then inhibition would not be seen when the isolated enzyme is treated with azide and would only occur in the presence of a substantial ΔP, explaining why this effect has not been previously described. This might suggest that azide binds to the membrane domain of the enzyme which contains the proton pumps and would be sensitive to the electric field generated by $\Delta\Psi$ rather than the electron transfer domain, which is outside the membrane and would not sense ΔP [44]. If this is the case, then this data suggests that functionality of complex I is good metric of function and can be used in future studies to investigate the effect of small molecules, mutations or post-translational modifications.

4.4. Complex IV driving force

Complex IV is the terminal acceptor of the ETC and pumps one proton per electron. The electrons from Cyt*c* are first transferred to the Cu_A centre just below the Cyt*c* binding site [45], then onto the heme *a* and finally to the binuclear centre (BNC) consisting of heme a_3 and the Cu_B centre, where oxygen is reduced to water. As opposed to the other complexes, complex IV operates far from equilibrium and so analysis in terms of the functionality is not appropriate. It has been shown that the turnover number of purified and detergent-solubilized complex IV respiring on Cyt*c* and ascorbate is proportional to the concentration of reduced Cyt*c* [46,47]. This was originally interpreted as turnover being limited by the binding and release of Cyt*c*. However, this has been questioned after it was found that the Cu_A centre remains in redox equilibrium with Cyt*c* [47]. A linear relationship between turnover and the ΔG was found in isolated mitochondria treated with an uncoupler [48,49] and, as would be expected for an enzyme which operates far from equilibrium, the relationship did not pass through the origin. In contrast, when respiration was titrated with an upstream inhibitor, the relationship was non-linear with ΔG and the gradient was negative such that turnover decreased as the reaction moved further from equilibrium [49]. In this paper, we used a null-point study to quantify the relative contribution of E_h^{Cytc} and ΔP to the turnover of CytOx and derive an empirical driving force of $E_h^{Cytc} + 1.23\Delta P$ for complex IV turnover. Surprisingly, we find a linear relationship between this driving force and turnover except at very low turnover numbers which, as would be expected, is not affected by piericidin. Our technique clearly demonstrates that inhibition by azide has a very different effect than inhibition by cyanide, in line with previous studies in the isolated enzyme. These have shown that azide acts as an uncompetitive inhibitor with regards to oxygen whereas cyanide acts as a non-competitive inhibitor; both being non-competitive with respect to Cyt*c* [41]. In line with this, optical and infrared spectroscopy have found two binding sites for azide in the oxidized enzyme: one with K_d of 64 μM in a protein environment, and the other with an K_d of 20 mM bound to a metal ion [50,51]. Similarly, the crystal structure also shows two azide binding sites, one at the periphery of subunit I far (16 Å) from both hemes where it is hydrogen bonded to amino acids (Tyr379 and Asn422), and one at the BNC bridging the iron of the heme and Cu_B [52]. We calculated a K_i of 74 μM in the cells with 300 μM of azide assuming inhibition is given by the fractional change in functionality. This is consistent with previous reported values of the K_i of azide (55 μM) in the isolated enzyme [41] and suggests that inhibition in the isolated enzyme and in our cells is caused by the binding to the peripheral site rather than the BNC. In contrast, titration studies have shown only one binding site for cyanide in the oxidase [53] which, according to the crystal structure, lies at the BNC [54,55]. Furthermore, it is known that cyanide can bind to the reduced enzyme (K_d of 100 μM) and to the oxidized enzyme in a two-step process (final K_d of 1 μM) [56]. The reduced cyanide-bound enzyme is still able to reduce oxygen to water [41], whereas the oxidized cyanide bound form cannot, even in the presence of reduced Cyt*c* [53]. Even though both azide and cyanide preferentially bind to the oxidized enzyme, their different binding sites could account for the different forms of inhibition observed in the isolated enzyme.

The results presented here suggest that the azide bound enzyme is catalytically incompetent thus changing the gradient (only the unbound form contributes to turnover) with little change in the x-axis intercept while the cyanide bound form, at these concentrations and under these conditions, is catalytically competent and can still reduce oxygen with a similar gradient but with a decreased x-axis crossing point. This is very different from a normal understanding of cyanide inhibition and requires further investigation.

4.5. Interpreting the driving force for complex IV

The form of the driving force and the observation that the turnover of complex IV is linear with the driving force invite an interpretation in terms of an energy transducing near-equilibrium system: the x-axis crossing point would be the redox potential of an apparent electron acceptor, the $1.23\Delta P$ would be the energy transduced, and the gradient would correspond to the functionality. The ΔG of this reaction would be given by:

$$\Delta G_{c\rightarrow Acc} = -(E_h^{Acc} - E_h^{Cytc}) + 1.23\Delta P \quad (7)$$

where E_h^{Acc} is the redox potential of the acceptor which is being maintained at redox potential of ≈563 mV. An obvious candidate for the electron acceptor is the binuclear centre. Proton pumping occurs on transfer of an electron from heme *a* to the BNC, consistent with the need for an energy transduction term. Furthermore, the proton pump is fully reversible [57,58] (only the oxygen reduction is irreversible) implying that the proton pump can operate close to equilibrium. Finally, binding of cyanide lowers the midpoint potential of heme a_3 [59] consistent with it lowering the redox potential of the BNC and decreasing the x-axis cross point. Although these facts give some credence to an energy transduction interpretation and identification of the BNC as the electron acceptor, the situation is more complicated. The BNC cycles though the states P, F, O, E and R with each transition requiring an electron from heme *a* and a substrate proton from the matrix. The fully reduced state, R, then binds molecular oxygen to form state A whereupon the oxygen undergoes a concerted and irreversible 4-electron reduction to regenerate P (see [60] for a review). Each electron transferred to the BNC

is accompanied by the pumping of one proton and movement of another charge across the membrane (an electron is transferred from Cyt*c* to the BNC and the substrate proton is taken up from the matrix to the BNC) giving an energy transduction of $\Delta P + \Delta\Psi$, very different from $1.23\Delta P$. Furthermore, the midpoint potential of the P/F and F/O couples is much higher than 560 mV [61] whereas the E/R couple is much lower at ≈340 mV when measured in redox titrations [59]. It has been noted that the low midpoint potential of the E/R couple is insufficient to pump protons and it must have a higher midpoint potential in-vivo [62]. If the apparent electron acceptor is the BNC, then this would be the first direct observation of this higher midpoint potential.

4.6. Oxygen consumption and ΔP

In the present work we measured the impact of mitochondrial inhibition on oxygen consumption and, being able to quantitate Δ*P*, we are also able to investigate how these two parameters vary. We found that inhibition of complex I with piericidin leads to a decrease in oxygen consumption with little change in Δ*P* whereas inhibition of complex IV with cyanide or azide leads to a more moderate decrease in oxygen consumption but a greater decrease in Δ*P* (Fig. 2h).

It seems obvious that an inhibition of the ETC would lead to a decrease in oxygen consumption. However, if the rate of ATP consumption by the cytosol is constant, and hence the rate of proton influx through the ATP synthase is constant, then the instantaneous decrease in both electron flux and proton pumping upon partial inhibition of the ETC would lead to a decrease in Δ*P* due to the mismatch in proton efflux and influx. This decrease in Δ*P* would drive the pumping complexes away from equilibrium and thereby increase both electron flux and rate of proton pumping until a new steady state is achieved. This new steady state would occur when the proton pumping rate matches the unchanged proton influx through the ATP synthase, and so the resulting oxygen consumption will not have changed but Δ*P* will have decreased. However, we do see a decrease in oxygen consumption implying that cytosolic ATP consumption has decreased. One possible explanation is that the decrease in Δ*P* leads to a decrease in cytosolic ΔG_{ATP} which is sensed by the ATP consuming reactions, resulting in a decrease in the rate of cytosolic ATP consumption. In parallel, the decrease in ΔG_{ATP} could be sensed by the glycolytic enzymes, triggering an increase in glycolytic ATP production and therefore decreasing the need for mitochondrial ATP. Consistent with this, in addition to mass action and allosteric binding of ADP and ATP, AMPK is sensitive to the square of the ADP/ATP ratio and has downstream targets which decrease ATP usage and increase glycolysis [63].

Within this framework, the effect of inhibiting the ETC on Δ*P* and oxygen consumption should be independent of the site of that inhibition, which is not what we observe. Our results imply that the ATP consumption in the cytosol is regulated by an additional pathway or pathways that can somehow sense the site of inhibition and preferentially decrease ATP demand on inhibition of complex I. This would complicate the interpretation of the control coefficients in metabolic control analysis.

4.7. Determining maximal respiratory rate

The oxygen consumption of cells treated with a protonophore is commonly used as a measure of the maximal oxygen consumption [64] and the data presented here can determine what limits the maximum respiratory rate. The addition of the protonophore increases the leak through the inner membrane and lowers Δ*P*, which in turn drives each pumping complex further from equilibrium and so increases their flux. Under baseline conditions the turnover number of complex III and IV are 138 e/s/complex III and 11.2 O_2/s/complex IV, respectively, putting them centrally in the linear region of the force flux relationship. Given the functionality, each millivolt decrease in Δ*P* will increase the flux through complex I, III and IV by ≈8, 10 and 6 e/complex III/s, respectively, in untreated cells. The value for complex III was calculated assuming Δ*pH* was constant and the value for complex IV was converted to e^-/complex III using the content of complex IV to complex III ratio (3.1 ± 0.1) and $4e^-/O_2$. The flux through all the complexes must be the same in the new steady state and this requires changes in the redox spans due to changes in the redox potentials of the intermediate redox pools.

If the redox potential of the NADH/NAD^+ pool were fixed, the greater pre-steady state flux through complex III would oxidize the UQH_2/UQ pool and reduce the Cyt*c* pool leading to a higher redox span across complex I, a lower span across complex III and a greater driving force for complex IV which would equalize the flux through each complex. However, Fig. 4 shows that the Cyt*c* pool is constant through much of the dynamic range of flux. In this case, the higher pre-steady state flux through complex III would oxidize the UQH_2/UQ pool decreasing the redox span across complex III and lowering the flux until it matched that of complex IV. Likewise the higher pre-steady state flux through complex I would oxidize the NADH/NAD^+ pool but the oxidation would have to be greater than the oxidation in the UQH_2/UQ pool in order to decrease the redox span and decrease the flux to match that through complex III and IV. The net result would be an oxidation in the UQH_2/UQ pool, a larger oxidation in the NADH/NAD^+ pool and decreased redox span across complex I and III, as is observed (Fig. 4). This pattern continues from the oligomycin inhibited state with increasing protonophore until the electron flux reaches ≈250 e/Complex III/s whereupon the Cyt*c* pool begins to oxidize because the force-flux relationship of complex III begins to saturate and the redox span increases to maintain flux. This oxidation decreases the driving force for complex IV requiring a larger decrease in Δ*P* to elicit the same increase in flux. At ≈275 e/Complex III/s, the UQH_2/UQ pool begins to oxidize at a higher rate as complex I begins to saturate. At this point, further addition of protonophore leads to a decline in $\Delta\Psi$ and an oxidation in Cyt*c* without further changing electron flux.

Although complex III saturates first, the maximal respiration rate is not limited by the activity of complex III because the *in-silico* modelling shows that much higher fluxes can be created with a different redox poise. Instead it is the oxidation in the UQH_2/UQ pool which causes flux through complex III to saturate. This oxidation is, in large part, due to the oxidation in the NADH/NAD^+ pool. The simplest explanation for the oxidation in the NADH/NAD^+ pool is that this is necessary to increase the rate of the TCA cycle through mass action. However, a similar oxidation is also observed in the state 4 to state 3 transition when isolated mitochondria respire on malate and glutamate, which presumably uses the malate-aspartate shuttle and only the malate dehydrogenase segment of the TCA cycle.

5. Conclusions

In this paper we have developed an alternative framework for understanding ETC flux and regulation under physiological conditions. We have shown that the functionality of complex I can be used to detect changes complex I function upon inhibition by piericidin and azide, that caution needs to be employed in interpreting the functionality of complex III and we have developed a similar metric for complex IV which can differentiate the effects of inhibition by cyanide and azide. Currently, post-translational modifications are particularly difficult to quantify in isolated systems because the changes are often lost on purification and the kinase and phosphatase inhibitors, which are used to preserve protein phosphorylation during isolation, are also potent inhibitors of oxidative phosphorylation. These measurements should be a powerful tool in quantifying regulation by post translational modification, different subunit isoforms and DNA mutations that lead to mitochondrial diseases.

Transparency document

The Transparency document associated with this article can be found, in online version.

Acknowledgements

We are grateful to Justin Fedor at the MRC Mitochondrial Biology Unit, Cambridge, UK for determining the level of azide inhibition on complex I.

References

[1] P. Mitchell, Keilin's respiratory chain concept and its chemiosmotic consequences, Science 206 (4423) (1979) 1148–1159.
[2] N. Soga, K. Kimura, K. Kinosita Jr., M. Yoshida, T. Suzuki, Perfect chemomechanical coupling of FoF1-ATP synthase, Proc. Natl. Acad. Sci. U. S. A. 114 (19) (2017) 4960–4965.
[3] P.C. Hinkle, M.A. Kumar, A. Resetar, D.L. Harris, Mechanistic stoichiometry of mitochondrial oxidative phosphorylation, Biochemistry 30 (14) (1991) 3576–3582.
[4] M.D. Brand, L.F. Chien, P. Diolez, Experimental discrimination between proton leak and redox slip during mitochondrial electron transport, Biochem. J. 297 (Pt 1) (1994) 27–29.
[5] R.S. Balaban, Domestication of the cardiac mitochondrion for energy conversion, J. Mol. Cell. Cardiol. 46 (2009) 832–841.
[6] J.P. Mazat, S. Ransac, M. Heiske, A. Devin, M. Rigoulet, Mitochondrial energetic metabolism-some general principles, IUBMB Life 65 (3) (2013) 171–179.
[7] D.G. Nicholls, The influence of respiration and ATP hydrolysis on the proton-electrochemical gradient across the inner membrane of rat-liver mitochondria as determined by ion distribution, Eur. J. Biochem. 50 (1) (1974) 305–315.
[8] B. Chance, G.R. Williams, Respiratory enzymes in oxidative phosphorylation. III. The steady state, J. Biol. Chem. 217 (1) (1955) 409–427.
[9] D.M. Kirby, D.R. Thorburn, D.M. Turnbull, R.W. Taylor, Biochemical assays of respiratory chain complex activity, Methods Cell Biol. 80 (2007) 93–119.
[10] J.G. Fedor, A.J.Y. Jones, A. Di Luca, V.R.I. Kaila, J. Hirst, Correlating kinetic and structural data on ubiquinone binding and reduction by respiratory complex I, Proc. Natl. Acad. Sci. U. S. A. 114 (48) (2017) 12737–12742.
[11] K. Blinova, S. Carroll, S. Bose, A.V. Smirnov, J.J. Harvey, J.R. Knutson, R.S. Balaban, Distribution of mitochondrial NADH fluorescence lifetimes: steady-state kinetics of matrix NADH interactions, Biochemistry 44 (7) (2005) 2585–2594.
[12] A.J. Jones, J.N. Blaza, H.R. Bridges, B. May, A.L. Moore, J. Hirst, A self-assembled respiratory chain that catalyzes NADH oxidation by ubiquinone-10 cycling between complex I and the alternative oxidase, Angew. Chem. Int. Ed. Eng. 55 (2) (2016) 728–731.
[13] Q.S. Zhu, J.A. Berden, S. De Vries, E.C. Slater, On the role of ubiquinone in the respiratory chain, Biochim. Biophys. Acta 680 (1) (1982) 69–79.
[14] H. Tian, R. Sadoski, L. Zhang, C.A. Yu, L. Yu, B. Durham, F. Millett, Definition of the interaction domain for cytochrome c on the cytochrome bc(1) complex. Steady-state and rapid kinetic analysis of electron transfer between cytochrome c and *Rhodobacter sphaeroides* cytochrome bc(1) surface mutants, J. Biol. Chem. 275 (13) (2000) 9587–9595.
[15] N. Kim, M.O. Ripple, R. Springett, Measurement of the mitochondrial membrane potential and pH gradient from the redox poise of the Hemes of the bc1 complex, Biophys. J. 102 (7) (2012) 1194–1203.
[16] P. Nicholls, Cytochrome c binding to enzymes and membranes, Biochim. Biophys. Acta 346 (3–4) (1974) 261–310.
[17] K.J. van Buuren, B.F. van Gelder, T.A. Eggelte, Biochemical and biophysical studies on cytochrome aa 3. I. Steady-state kinetics of cytochrome aa 3, Biochim. Biophys. Acta 234 (3) (1971) 468–480.
[18] C.A. Sinkler, H. Kalpage, J. Shay, I. Lee, M.H. Malek, L.I. Grossman, M. Huttemann, Tissue- and condition-specific isoforms of mammalian cytochrome c oxidase subunits: from function to human disease, Oxidative Med. Cell. Longev. 2017 (2017) 1534056.
[19] I. Lee, A.R. Salomon, S. Ficarro, I. Mathes, F. Lottspeich, L.I. Grossman, M. Huttemann, cAMP-dependent tyrosine phosphorylation of subunit I inhibits cytochrome c oxidase activity, J. Biol. Chem. 280 (7) (2005) 6094–6100.
[20] V.A. Morais, D. Haddad, K. Craessaerts, P.J. De Bock, J. Swerts, S. Vilain, L. Aerts, L. Overbergh, A. Grunewald, P. Seibler, C. Klein, K. Gevaert, P. Verstreken, B. De Strooper, PINK1 loss-of-function mutations affect mitochondrial complex I activity via NdufA10 ubiquinone uncoupling, Science 344 (6180) (2014) 203–207.
[21] A. Galkin, S. Moncada, Modulation of the conformational state of mitochondrial complex I as a target for therapeutic intervention, Interface Focus 7 (2) (2017) 20160104.
[22] M.O. Ripple, N. Kim, R. Springett, Mammalian complex I pumps 4 protons per 2 electrons at high and physiological proton motive force in living cells, J. Biol. Chem. 288 (8) (2013) 5374–5380.
[23] M.O. Ripple, N. Kim, R. Springett, Acute mitochondrial inhibition by mitogen-activated protein kinase/extracellular signal-regulated kinase kinase (MEK) 1/2 inhibitors regulates proliferation, J. Biol. Chem. 288 (5) (2013) 2933–2940.
[24] N. Kim, M.O. Ripple, R. Springett, Spectral components of the alpha-band of cytochrome oxidase, Biochim. Biophys. Acta 1807 (7) (2011) 779–787.
[25] B.M. Kenwood, J.L. Weaver, A. Bajwa, I.K. Poon, F.L. Byrne, B.A. Murrow, J.A. Calderone, L. Huang, A.S. Divakaruni, J.L. Tomsig, K. Okabe, R.H. Lo, G. Cameron Coleman, L. Columbus, Z. Yan, J.J. Saucerman, J.S. Smith, J.W. Holmes, K.R. Lynch, K.S. Ravichandran, S. Uchiyama, W.L. Santos, G.W. Rogers, M.D. Okusa, D.A. Bayliss, K.L. Hoehn, Identification of a novel mitochondrial uncoupler that does not depolarize the plasma membrane, Mol. Metab. 3 (2) (2014) 114–123.
[26] B.L. Trumpower, The protonmotive Q cycle. Energy transduction by coupling of proton translocation to electron transfer by the cytochrome bc1 complex, J. Biol. Chem. 265 (20) (1990) 11409–11412.
[27] A.R. Crofts, S.W. Rose, R.L. Burton, A.V. Desai, P.J.A. Kenis, S.A. Dikanov, The Q-cycle mechanism of the bc1 complex: a biologist's perspective on atomistic studies, J. Phys. Chem. B 121 (15) (2017) 3701–3717.
[28] R. Springett, Novel methods for measuring the mitochondrial membrane potential, Methods Mol. Biol. 1264 (2015) 195–202.
[29] V.P. Shinkarev, A.R. Crofts, C.A. Wraight, The electric field generated by photosynthetic reaction center induces rapid reversed electron transfer in the bc1 complex, Biochemistry 40 (42) (2001) 12584–12590.
[30] P.M. Wood, The potential diagram for oxygen at pH 7, Biochem. J. 253 (1) (1988) 287–289.
[31] M. Degli Esposti, A. Ghelli, M. Crimi, E. Estornell, R. Fato, G. Lenaz, Complex I and complex III of mitochondria have common inhibitors acting as ubiquinone antagonists, Biochem. Biophys. Res. Commun. 190 (3) (1993) 1090–1096.
[32] S. Ransac, J.P. Mazat, How does antimycin inhibit the bc(1) complex? A part-time twin, Biochim. Biophys. Acta 1797 (2010) 1849–1857.
[33] E. Darrouzet, C.C. Moser, P.L. Dutton, F. Daldal, Large scale domain movement in cytochrome bc(1): a new device for electron transfer in proteins, Trends Biochem. Sci. 26 (7) (2001) 445–451.
[34] S. Ransac, N. Parisey, J.P. Mazat, The loneliness of the electrons in the bc1 complex, Biochim. Biophys. Acta 1777 (7–8) (2008) 1053–1059.
[35] A. Osyczka, C.C. Moser, P.L. Dutton, Fixing the Q cycle, Trends Biochem. Sci. 30 (4) (2005) 176–182.
[36] A.R. Crofts, Proton-coupled electron transfer at the Qo-site of the bc1 complex controls the rate of ubihydroquinone oxidation, Biochim. Biophys. Acta 1655 (1–3) (2004) 77–92.
[37] D. Victoria, R. Burton, A.R. Crofts, Role of the -PEWY-glutamate in catalysis at the Q (o)-site of the Cyt bc(1) complex, Biochim. Biophys. Acta 1827 (3) (2013) 365–386.
[38] C.A. Wilson, A.R. Crofts, Dissecting the pattern of proton release from partial process involved in ubihydroquinone oxidation in the Q-cycle, Biochim. Biophys. Acta 1859 (7) (2018) 531–543.
[39] B. Glancy, W.T. Willis, D.J. Chess, R.S. Balaban, Effect of calcium on the oxidative phosphorylation cascade in skeletal muscle mitochondria, Biochemistry 52 (16) (2013) 2793–2809.
[40] R. Covian, S. French, H. Kusnetz, R.S. Balaban, Stimulation of oxidative phosphorylation by calcium in cardiac mitochondria is not influenced by cAMP and PKA activity, Biochim. Biophys. Acta 1837 (12) (2014) 1913–1921.
[41] L.C. Petersen, P. Nicholls, H. Degn, The effect of oxygen concentration on the steady-state kinetics of the solubilized cytochrome c oxidase, Biochim. Biophys. Acta 452 (1) (1976) 59–65.
[42] M.W. Bowler, M.G. Montgomery, A.G. Leslie, J.E. Walker, How azide inhibits ATP hydrolysis by the F-ATPases, Proc. Natl. Acad. Sci. U. S. A. 103 (23) (2006) 8646–8649.
[43] K. Bogucka, L. Wojtczak, Effect of sodium azide on oxidation and phosphorylation processes in rat-liver mitochondria, Biochim. Biophys. Acta 122 (3) (1966) 381 (&).
[44] R. Baradaran, J.M. Berrisford, G.S. Minhas, L.A. Sazanov, Crystal structure of the entire respiratory complex I, Nature 494 (7438) (2013) 443–448.
[45] S. Shimada, K. Shinzawa-Itoh, J. Baba, S. Aoe, A. Shimada, E. Yamashita, J. Kang, M. Tateno, S. Yoshikawa, T. Tsukihara, Complex structure of cytochrome c-cytochrome c oxidase reveals a novel protein-protein interaction mode, EMBO J. 36 (3) (2017) 291–300.
[46] H. Conrad, L. Smith, A study of the kinetics of the oxidation of cytochrome c by cytochrome c oxidase, Arch. Biochem. Biophys. 63 (2) (1956) 403–413.
[47] M.G. Mason, P. Nicholls, C.E. Cooper, The steady-state mechanism of cytochrome c oxidase: redox interactions between metal centres, Biochem. J. 422 (2) (2009) 237–246.
[48] M.P. Murphy, G.C. Brown, M.D. Brand, Thermodynamic limits to the stoichiometry of H+ pumping by mitochondrial cytochrome oxidase, FEBS Lett. 187 (1) (1985) 16–20.
[49] M.P. Murphy, M.D. Brand, The control of electron flux through cytochrome oxidase, Biochem. J. 243 (2) (1987) 499–505.
[50] W. Li, G. Palmer, Spectroscopic characterization of the interaction of azide and thiocyanate with the binuclear center of cytochrome oxidase: evidence for multiple ligand sites, Biochemistry 32 (7) (1993) 1833–1843.
[51] S. Yoshikawa, W.S. Caughey, Infrared evidence of azide binding to iron, copper, and non-metal sites in heart cytochrome c oxidase, J. Biol. Chem. 267 (14) (1992) 9757–9766.
[52] M.J. Fei, E. Yamashita, N. Inoue, M. Yao, H. Yamaguchi, T. Tsukihara, K. Shinzawa-Itoh, R. Nakashima, S. Yoshikawa, X-ray structure of azide-bound fully oxidized cytochrome c oxidase from bovine heart at 2.9 A resolution, Acta Crystallogr. D Biol. Crystallogr. 56 (Pt 5) (2000) 529–535.
[53] P. Nicholls, K.J. van Buuren, B.F. van Gelder, Biochemical and biophysical studies on cytochrome aa 3. 8. Effect of cyanide on the catalytic activity, Biochim. Biophys. Acta 275 (3) (1972) 279–287.
[54] K. Muramoto, K. Ohta, K. Shinzawa-Itoh, K. Kanda, M. Taniguchi, H. Nabekura, E. Yamashita, T. Tsukihara, S. Yoshikawa, Bovine cytochrome c oxidase structures enable O2 reduction with minimization of reactive oxygens and provide a proton-pumping gate, Proc. Natl. Acad. Sci. U. S. A. 107 (17) (2010) 7740–7745.

[55] N. Yano, K. Muramoto, M. Mochizuki, K. Shinzawa-Itoh, E. Yamashita, S. Yoshikawa, T. Tsukihara, X-ray structure of cyanide-bound bovine heart cytochrome c oxidase in the fully oxidized state at 2.0 A resolution, Acta Crystallogr. Sect. F Struct. Biol. Cryst. Commun. 71 (Pt 6) (2015) 726–730.
[56] K.J. van Buuren, P. Nicholls, B.F. van Gelder, Biochemical and biophysical studies on cytochrome aa 3. VI. Reaction of cyanide with oxidized and reduced enzyme, Biochim. Biophys. Acta 256 (2) (1972) 258–276.
[57] M. Wikstrom, Energy-dependent reversal of the cytochrome oxidase reaction, Proc. Natl. Acad. Sci. U. S. A. 78 (7) (1981) 4051–4054.
[58] M. Wikstrom, J.E. Morgan, The dioxygen cycle, Spectral, kinetic, and thermodynamic characteristics of ferryl and peroxy intermediates observed by reversal of the cytochrome oxidase reaction, J. Biol. Chem. 267 (15) (1992) 10266–10273.
[59] N. Kojima, G. Palmer, Further characterization of the potentiometric behavior of cytochrome oxidase. Cytochrome alpha stays low spin during oxidation and reduction, J. Biol. Chem. 258 (24) (1983) 14908–14913.
[60] I. Belevich, M.I. Verkhovsky, Molecular mechanism of proton translocation by cytochrome c oxidase, Antioxid. Redox Signal. 10 (1) (2008) 1–29.
[61] G.T. Babcock, M. Wikstrom, Oxygen activation and the conservation of energy in cell respiration, Nature 356 (6367) (1992) 301–309.
[62] D. Bloch, I. Belevich, A. Jasaitis, C. Ribacka, A. Puustinen, M.I. Verkhovsky, M. Wikstrom, The catalytic cycle of cytochrome c oxidase is not the sum of its two halves, Proc. Natl. Acad. Sci. U. S. A. 101 (2) (2004) 529–533.
[63] D.G. Hardie, Minireview: the AMP-activated protein kinase cascade: the key sensor of cellular energy status, Endocrinology 144 (12) (2003) 5179–5183.
[64] M.D. Brand, D.G. Nicholls, Assessing mitochondrial dysfunction in cells, Biochem. J. 435 (2) (2011) 297–312.